JOURNAL OF SPACECRAFT AND ROCKETS
Vol. 35, No. 2, March–April 1998

Exploring the Validity of the Spalart–Allmaras Turbulence Model for Hypersonic Flows

R. Paciorri,* W. Dieudonné,† G. Degrez,‡ J.-M. Charbonnier,§ and H. Deconinck¶
von Kármán Institute for Fluid Dynamics, 1640 Sint-Genesius-Rode, Belgium

The Spalart–Allmaras turbulence model has been implemented in a finite volume code using an implicit finite difference technique. First, the implementation was validated on flat plate turbulent boundary-layer flows under various flow conditions. Then, three high-speed flow applications characterized by different turbulent phenomena were considered to investigate the behavior of the Spalart–Allmaras model in the hypersonic regime, namely, a hypersonic wind-tunnel flow, a Mach 5 flow over a hollow-cylinder flare, and a Mach 6.8 flow over a hyperboloid flare. Numerical results were found in excellent agreement with experimental data for the attached nozzle flow and the hyperboloid flow involving laminar separation and turbulent reattachment. For the hollow-cylinder flare configuration, which involves turbulent separation, the magnitudes of surface pressure and of heat transfer peaks were correctly predicted, whereas their positions were slightly incorrect due to the underprediction of the separation bubble size.

Nomenclature

b_{dest} = destruction term, $\text{m}^2\ \text{s}^{-2}$
b_{prod} = production term, $\text{m}^2\ \text{s}^{-2}$
b_{trip} = trip term, $\text{m}^2\ \text{s}^{-2}$
c_f = skin-friction coefficient
c_p = pressure coefficient
d = distance to the wall, m
d_T = distance to the transition point, m
M = Mach number
P = pressure, Nm^{-2}
P_t = pitot pressure, Nm^{-2}
Pr = Prandtl number
R = gas constant, $\text{J kg}^{-1}\ \text{K}^{-1}$
Re_1 = unit Reynolds number, m^{-1}
S = vorticity, s^{-1}
St = Stanton number
T = temperature, K
u = velocity component, m s^{-1}
y^+ = distance normal to the wall expressed in wall units
γ = ratio of specific heats
μ = dynamic viscosity, $\text{kg m}^{-1}\ \text{s}^{-1}$
ν = kinematic viscosity, $\text{m}^2\ \text{s}^{-1}$
ρ = density, kg m^{-3}
σ = turbulent Prandtl number

Subscripts

i, j, k = coordinate index
T = turbulent
w = wall
0 = reservoir conditions
∞ = freestream

Introduction

TURBULENCE modeling plays an important role in hypersonic flow computations. Because turbulent flows are present in many hypersonic applications, it is often necessary to include a turbulence model in the flow modeling. Nevertheless, the turbulence models developed in the past do not behave well in many situations present in hypersonic flows, and big differences exist between the computed solutions and the experimental data.[1]

A new family of turbulence models based on one differential equation was recently introduced by Baldwin and Barth.[2] The Spalart–Allmaras model[3] represents the latest evolution of this class of models. This family does not follow the classical Prandtl approach, where the model equation is obtained from the turbulent kinetic energy equation. In particular, the Baldwin–Barth model derives the equation from the k–ϵ model, whereas in the Spalart–Allmaras model, the equation is generated from scratch using empiricism and arguments of dimensional analysis, Galilean invariance, and selective dependence on the molecular viscosity.

The Spalart–Allmaras model has been implemented by many groups, providing good results in a wide range of different applications.[4] Nevertheless, the behavior of this new turbulence model in hypersonic flow has not been adequately explored. The purpose of the present study is to review its performance in the hypersonic regime.

Model

The Spalart–Allmaras model belongs to the family of eddy viscosity models. This family of models is based on the assumption that the Reynolds stress tensor $-\overline{\rho u_i' u_j'}$ is related to the mean strain rate through an apparent turbulent viscosity, called eddy viscosity ν_T:

$$-\overline{\rho u_i' u_j'} = \bar{\rho}\nu_T\left(\frac{\partial \tilde{u}_i}{\partial y^j} + \frac{\partial \tilde{u}_j}{\partial y^i}\right) \tag{1}$$

In the Spalart–Allmaras model, the eddy viscosity is computed through a partial differential equation. In particular, the eddy viscosity ν_T is computed by an intermediate variable $\tilde{\nu}$ through the relation

$$\nu_T = \tilde{\nu} f_{v1}(\chi) \tag{2}$$

where χ is the ratio

$$\chi = \tilde{\nu}/\nu$$

and f_{v1} is a damping function. The intermediate variable $\tilde{\nu}$ is computed by solving a differential equation that can be written in compact form as

$$\frac{\mathrm{D}\tilde{\nu}}{\mathrm{D}t} = b_{\text{prod}}(S, \tilde{\nu}, d) - b_{\text{dest}}(\tilde{\nu}, d) + b_{\text{trip}}(d_T) + \frac{1}{\sigma}\left\{\nabla\cdot[(\nu+\tilde{\nu})\nabla\tilde{\nu}] + c_{b2}(\nabla\tilde{\nu})^2\right\} \tag{3}$$

Received May 22, 1997; presented as Paper 97-2023 at the AIAA 28th Fluid Dynamics Conference, Snowmass Village, CO, June 29–July 2, 1997; revision received Nov. 11, 1997; accepted for publication Nov. 12, 1997.

*Postdoctoral Research Fellow, Aeronautics/Aerospace Department; currently Assistant Professor, Department of Mechanics and Aeronautics, University of Rome "La Sapienza," Via Eudossiana, 18, 00184 Rome, Italy.
†Research Assistant, Aeronautics/Aerospace Department.
‡Associate Professor, Aeronautics/Aerospace Department. Senior Member AIAA.
§Assistant Professor, Aeronautics/Aerospace Department.
¶Professor, Aeronautics/Aerospace Department. Member AIAA.

where b_{trip} is a special source term that allows the specification of the laminar–turbulent transition point location. Although the transition onset point has to be user specified, the flow development in the transition region is built into the model through this trip source term. The quantities enclosed between the braces show the variables on which the various source terms mainly depend. The last term on the right-hand side is a diffusion term, and c_{b2} is a calibration constant. More details and an extensive discussion about the Spalart–Allmaras model are reported in Ref. 3.

Implementation

The model has been implemented in the von Kármán Institute (VKI) multiblock (VKI-MB) code, which is an existing two-dimensional/axisymmetric compressible Navier–Stokes solver based on an upwind finite volume technique[5,6] and includes both explicit and implicit time-stepping schemes. The turbulence equation (3) is discretized in space by finite differences over the dual mesh of the finite volume mesh, i.e., a mesh whose nodes are the centers of the cells used by the finite volume scheme, and marched in time using a point implicit time-stepping scheme. Convective terms are discretized using first-order upwind finite differences, whereas diffusion terms are discretized using central differences. The point implicit time integration scheme consists of applying a single Jacobi iteration on the linearized backward Euler time discretization of the space-discretized turbulence equation. More details about the implementation of the turbulence model in the VKI-MB code are reported in Ref. 7.

Results

Boundary-Layer Flows

To validate the turbulence model implementation, a number of flat plate boundary-layer calculations have been carried out and numerical results have been successfully compared with both experimental data and classical theories.[7] In particular, the computed skin-friction coefficient has been compared with Van Driest's correlation[8] for subsonic and supersonic flows over an adiabatic flat plate at $M_\infty = 0.3$, 2.0, and 6.0. To allow for the comparison with Van Driest's correlation, the molecular viscosity was assumed to vary as a power of the static temperature, with an exponent $\omega = 0.76$. The comparison is shown in Fig. 1, where the normalized computed skin-friction coefficient for $Re_x = 10^7$ is plotted as a function of Mach number. The agreement with Van Driest's correlation is seen to be quite satisfactory even if the numerical results tend to underestimate the analytical data. Note that two-equation models also show the same behavior.[9] For completeness, an additional computation was carried out using Sutherland's viscosity law at Mach 6.0. As seen in Fig. 1, the result is very close to that obtained with the power-law molecular viscosity approximation.

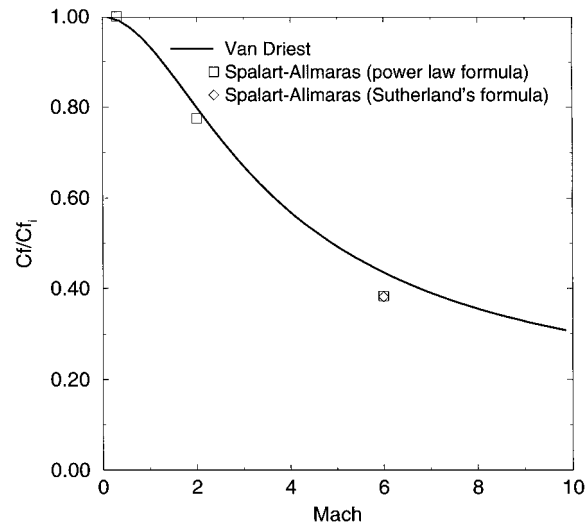

Fig. 1 Flat plate skin-friction coefficient for $Re_x = 10^7$; comparison of numerical results and Van Driest correlation.[8]

Table 1 LSCN1 operating condition

Testing gas	N_2
P_0, bar	900
T_0, K	2100
Nozzle length, m	1.694
Divergent angle, deg	6
Throat diameter, mm	5

Fig. 2 Mach number contours in VKI Longshot nozzle.

Wind-Tunnel Computation

The first application case considers a turbulent high-speed axisymmetric flow occurring in the VKI Longshot wind tunnel.[10] This facility is a free piston wind tunnel, which can provide flows at very high stagnation pressure levels (up to 4000 bar) and moderate temperatures (up to 2500 K). The Mach number of the flow in the test chamber can be changed from 14 to 20 using different nozzles (conical and contoured) and gases (N_2 and CO_2).[11] The computation to be presented reproduces an operating condition within the conical nozzle called LSCN1, where nitrogen (N_2) is used as the testing gas. The reservoir conditions and some geometrical parameters of the wind-tunnel nozzle are summarized in Table 1. Turbulent phenomena strongly influence the flow in the divergent part of the nozzle. Indeed, transition, which occurs downstream of the throat in an a priori unknown location, induces an important boundary-layer thickening. The resulting blockage effect significantly affects the flow development in the nozzle and, consequently, the flow conditions in the test section, as shown in Fig. 2, where the Mach number isolines of the computed solution are plotted.

Taking into account the low operating temperature of the gas in the wind tunnel, the flow is modeled by using the ideal gas model and the molecular viscosity is computed by means of Keyes' law. In view of the short running time (15 ms), the wall temperature of the wind tunnel is assumed to be uniform and equal to the pretest ambient value, i.e., 300 K. The solution has been computed on a sequence of three successively refined H grids with 269×41, 537×81, and 1073×161 points, respectively, which cover a computational domain extending from slightly upstream of the throat to the test section. Downstream of the nozzle exit plane, the freejet is assumed to grow conically and a slip boundary condition is applied at the jet boundary. Stretching was used at the wall with a normal cell dimension at the throat of 5×10^{-5}, 2.5×10^{-5}, and 1.25×10^{-5} mm for the coarse, medium, and fine grids, respectively. Practically identical heat transfer distributions were obtained on the medium and fine grids, indicating grid convergence.[12]

As already mentioned, the transition onset location is actually unknown. To determine it, three flow computations were performed with the transition onset point fixed at the throat and 0.15 and 0.30 m downstream, respectively. The normalized pitot pressures in the test section 20 mm downstream of the nozzle exit computed on the fine grid are compared with the experimental measurements, as well as with the results of a fully laminar computation, in Fig. 3. Laminar results are characterized by a thin shear layer and a low pitot pressure level in the test section, which is logical because a thinner wall boundary layer results in a higher Mach number in the core and, therefore, a smaller pitot pressure. The pitot pressure in the core is seen to be best matched with transition fixed at 0.3 m from the throat, whereas transition fixed at 0.15 m yields a shear layer thickness in closer agreement with the experimental data. Computed and measured heat flux distributions on the nozzle wall are compared in Fig. 4. Following the standard experimental procedure at VKI, they are normalized by the measured heat flux at the stagnation point of a 25.4-mm-radius hemispherical probe to account for slight variations in test conditions. It is seen that the transition point location has only a negligible effect on the wall heat flux in the turbulent region, and as all heat flux measurement points lie in the turbulent region, the comparison does not allow one to determine the actual transition point location.

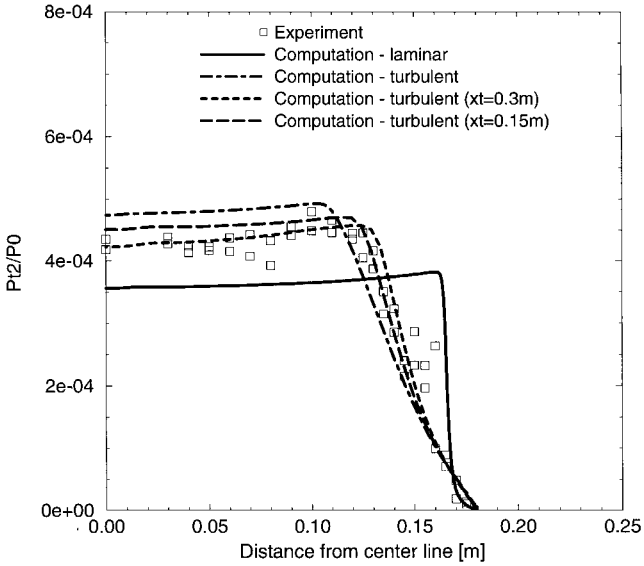

Fig. 3 Comparison of measured and computed normalized pitot pressures in test section.

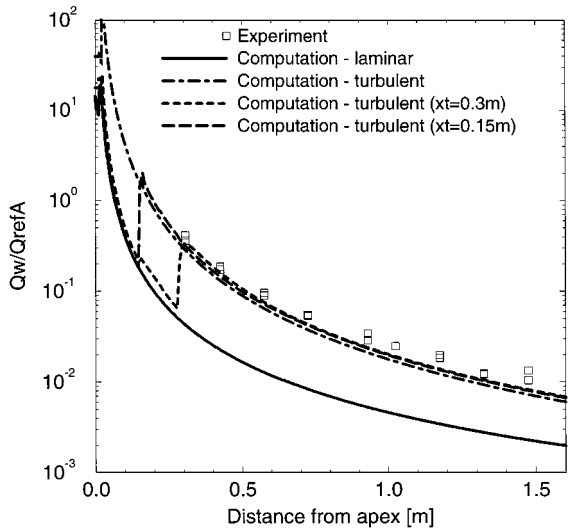

Fig. 4 Comparison of measured and computed nozzle wall heat flux distributions.

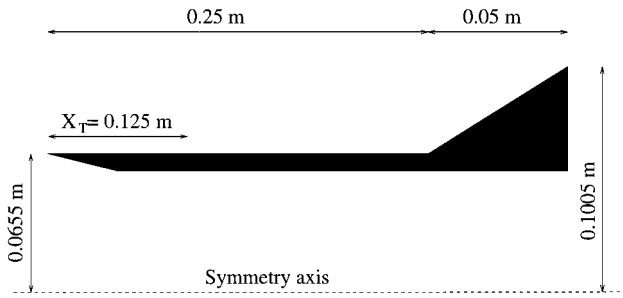

Fig. 5 Hollow-cylinder-flare geometry.

Hollow-Cylinder-Flare Computation

The second application corresponds to the Mach 5 flow over a hollow-cylinder flare. It was selected by AGARD-FDP Working Group 18 as a validation case.[13] The model consists of a 250-mm-long hollow cylinder with a sharp leading edge. At the end of the cylinder, a 35-deg flare is mounted (Fig. 5). The freestream flow conditions and other test case parameters are reported in Table 2.

The flow near the junction is characterized by a shock wave/boundary-layer interaction with a locally separated flow, a weak compression wave generated at the separation point, and a strong compression shock wave downstream of the reattachment point

Table 2 Hollow-cylinder flare test case

M_∞	5.01
T_0, K	500
P_0, Pa	3.5×10^6
T_w, K	300
μ	Sutherland's law
Transition, m	$X_T = 0.125$
Pr	0.72
Pr_T	0.90
Re_1, m^{-1}	4.41×10^7
R, J kg^{-1} K^{-1}	287
γ	1.4

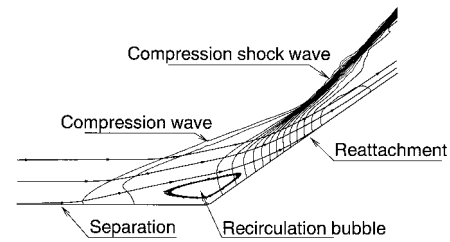

Fig. 6 Hollow-cylinder flare flowfield structure: pressure contours.

(Fig. 6). Turbulence plays an important role in this viscous interaction. In fact, the Reynolds number is sufficiently high ($Re_1 = 4.41 \times 10^7$ m^{-1}) to ensure a fully turbulent boundary layer upstream of the separation point. In the experiment, the turbulent transition occurs along the cylinder and the end of the transition region is approximately located at 125 mm from the leading edge. In the numerical computations, the beginning of the transition was fixed at 121 mm to account for the transition region length. The computed boundary-layer thickness just upstream of the interaction (220 mm downstream of the leading edge) was 2.1 mm.

The numerical solutions were computed on three different meshes. To start, a 100×50 mesh was used, after which the mesh was improved to obtain more accurate results. In particular, the first mesh adopts a constant wall stretching, whereas in the second one the wall stretching is adapted, taking into account the flow characteristics near the wall, as shown in Fig. 7. For this reason the second mesh assures a better wall discretization in the proximity and downstream of the reattachment point. This region is critical for the discretization. In fact, the boundary layer becomes very thin due to the high pressure in the reattachment point caused by the compression process. In addition, it is important to obtain a good solution in this zone because the pressure and heat flux peaks are located in this region. Figure 8 shows the y^+ values in the near wall points for both meshes. Although the meshes have the same number of cells, the value of y^+ does not exceed 2 in the second mesh, whereas in the first one y^+ is higher than 6. This means that, using the first mesh, no discretization points are placed in the viscous sublayer in proximity of the reattachment point. The effect of this mesh inadequacy on the solution accuracy is evident, observing the Stanton number distributions (Fig. 9). Of course, this lack of accuracy does not affect the pressure distribution because the pressure hardly depends on the near-wall boundary-layer behavior (Fig. 10).

Finally, the solution was computed on a 200×100 mesh based on the improved stretching. Figures 9 and 10 show the finest-mesh solution and the experimental data.[14] Concerning the Stanton number distribution, the agreement between the experimental data and the numerical results computed by using all of the meshes is excellent upstream of the separation point, whereas it is good downstream of the reattachment point only if the improved meshes are used. The numerical results do not match well with the experimental data in the separated flow region. Even if the magnitude of the heat flux peak is well estimated, its position is not correct because the size of the recirculation bubble is underpredicted. The comparison of the pressures exhibits the same behavior except downstream of the reattachment point, where the difference between the experimental and numerical data is larger.

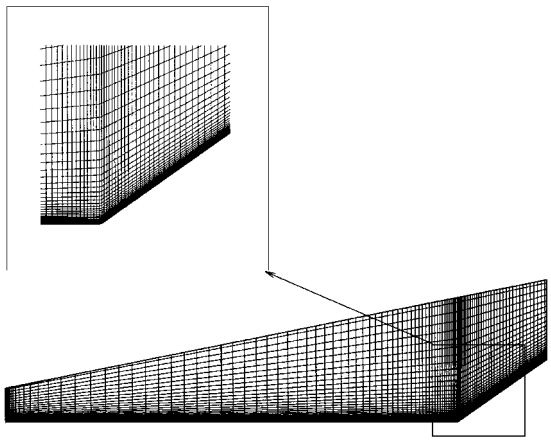

First-attempt mesh (100 × 50)

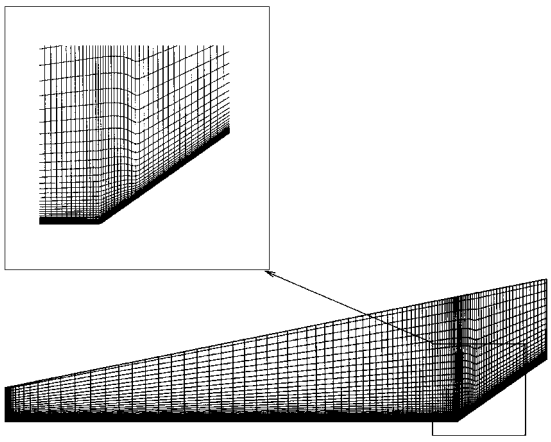

Improved mesh (100 × 50)

Fig. 7 Coarse grids for hollow-cylinder-flare problem.

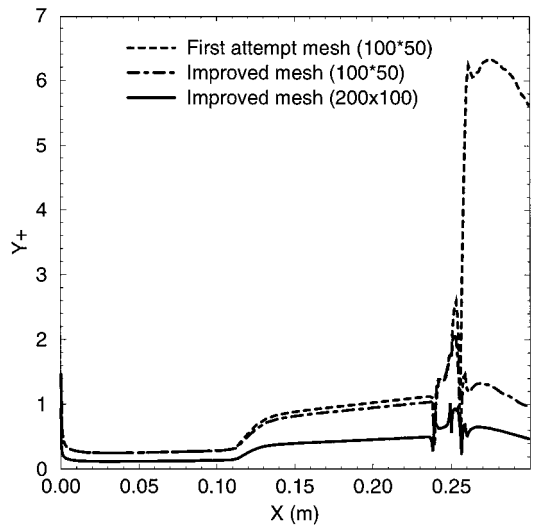

Fig. 8 Hollow-cylinder flare: y^+ distributions.

As pointed out in Ref. 1, there exist at least two reasons for the discrepancies between computational and experimental results, in particular regarding the separation bubble size. First, shock wave/turbulent boundary-layer interactions such as the present one are known to be highly unsteady, involving large-amplitude shock wave motions[15] that are not captured by Reynolds-averaged Navier–Stokes computations. Second, eddy viscosity models use a single length scale to characterize the turbulence characteristics. Whereas this is valid for attached boundary layer flow, it ceases to be correct in the presence of separation bubbles. In addition, the Spalart–Allmaras model, like many turbulence models, uses near-wall damping functions that lose their validity in the neighborhood of two-dimensional separation and reattachment points.

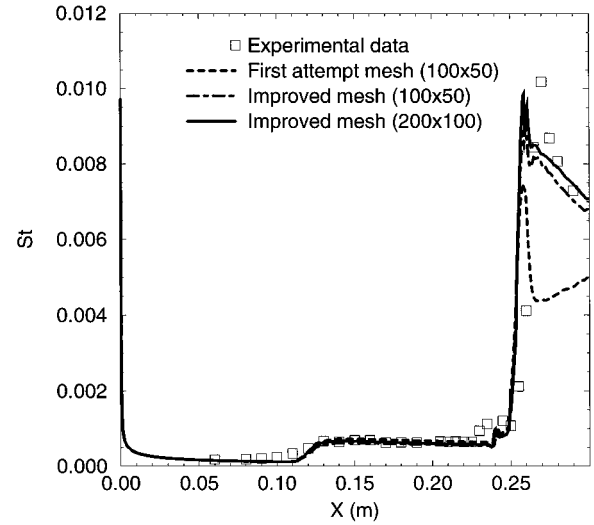

Fig. 9 Hollow-cylinder flare: Stanton number distribution.

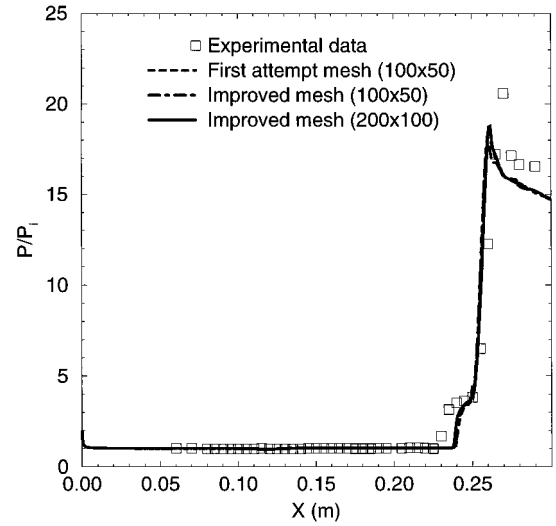

Fig. 10 Hollow-cylinder flare: wall pressure coefficient distribution.

Hyperboloid-Flare Computation

The last application case considers the flow over a hyperboloid flare tested in the DLR, German Aerospace Research Establishment, DLR-RWG wind tunnel.[16] The model geometry, defined in Ref. 17, is an axially symmetric geometry whose meridian shape is the windward centerline of the Hermes spacecraft at 30-deg angle of attack and with a 20-deg body flap deflection. The flow conditions in the test chamber and other parameters concerning this test case, known as the high-Reynolds-number case, are reported in Table 3. This computation was performed as VKI's contribution to the 1996 European Space Agency/European Space Research and Technology Center Workshop on Reentry Aerothermodynamics.[18,19] As in the hollow-cylinder-flare flow, a complex flow structure exists near the junction of the hyperboloid with the flare, such as a shock/boundary layer interaction and recirculatory flow. Contrary to the earlier test case, the flow in this region is not completely turbulent. In fact, turbulent transition occurs downstream of the separation point in a location that is unknown.

To investigate the effect of transition, three flow cases were computed, namely, a fully laminar flow and two turbulent flows with the transition point fixed, respectively, at separation and reattachment. Three grids of increasing refinement were used for each flow case, i.e., 101 × 26, 201 × 51, and 401 × 101 grids. The medium grid is shown in Fig. 11. The mesh stretching was such that y^+ did not exceed 3 on the fine mesh for all three flow cases, as shown in Fig. 12.

Table 3 High-Reynolds-number test case

Testing gas	Air
M_∞	6.85
T_0, K	600
P_0, Pa	3.25×10^6
T_w, K	300
Pr	0.72
Pr_T	0.90
Re_1, m^{-1}	14.8×10^6

Fig. 11 Hyperboloid-flare computation: medium (201 × 51) grid.

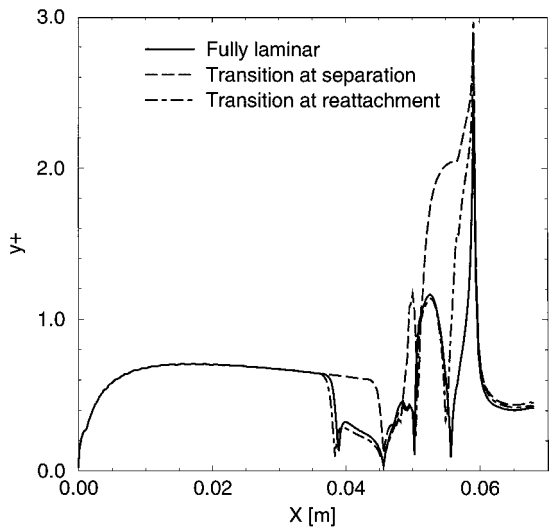

Fig. 12 Hyperboloid-flare computation: y^+ distributions on fine mesh.

Grid sensitivity is shown in Fig. 13 for the turbulent flow with transition fixed at reattachment. Although not perfectly identical, the medium- and fine-mesh distributions are sufficiently close that the fine-grid computation may be considered practically grid converged.

For the turbulent flow cases, running the Spalart–Allmaras model from an initial uniform flow did not provide a correct solution as the trip term was not sufficiently large to trigger a proper turbulence buildup, so that the flow remained essentially laminar. This problem was mentioned by the authors of the model in Ref. 3, and they suggested increasing the value of the constant that multiplies the trip term. Another strategy was used in the present work. A first approximation of the turbulent viscosity was computed using the algebraic Baldwin–Lomax model,[20] which served to initialize the intermediate variable $\tilde{\nu}$ (Ref. 18). An additional benefit of this procedure is that it dramatically reduces the CPU time to convergence.

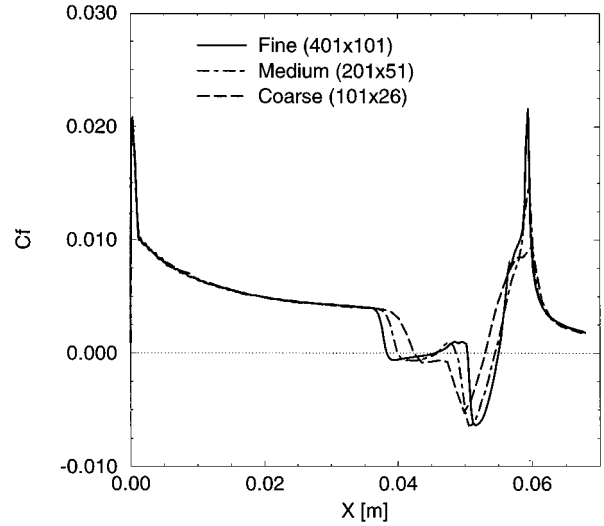

Fig. 13 Hyperboloid-flare computation: skin friction coefficient distributions on three grids (case with transition at reattachment).

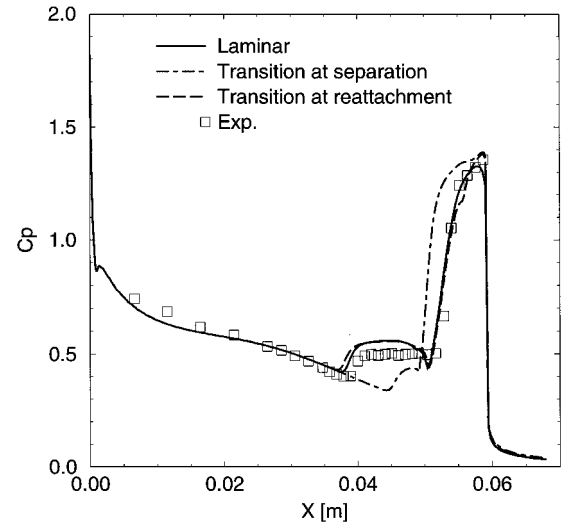

Fig. 14 Hyperboloid-flare computation: fine-grid pressure coefficient distributions.

In fact, in this way the long transient time that the Spalart–Allmaras model requires to produce a high-enough turbulent viscosity level needed to activate the production term downstream of the trip point is eliminated.

The fine-grid pressure coefficient and Stanton number distributions for the three flow cases are shown together with experimental data in Figs. 14 and 15. It is observed that fixing the transition point at separation results in a much too small separation bubble, so that it can be safely concluded that transition takes place downstream of separation. On the other hand, fixing transition at reattachment, the Stanton number distribution changes remarkably downstream of reattachment with respect to laminar computation. In particular, it strongly enhances heat transfer. A similar behavior is shown by the skin-friction coefficient (Fig. 16). The peak heating magnitude is seen to be in excellent agreement with the experimental data, but the computed Stanton number rise is slightly downstream of the experimental one, suggesting that transition might actually take place somewhat upstream of reattachment. The pressure coefficient distribution also agrees quite well with the experimental data, except in the separated region, where the pressure level is overestimated, perhaps due to a slight overestimation of the separation bubble size, and is seen to be essentially insensitive to the boundary-layer state downstream of reattachment. Finally, the skin-friction coefficient distribution reveals the existence of a secondary separation bubble (Fig. 16).

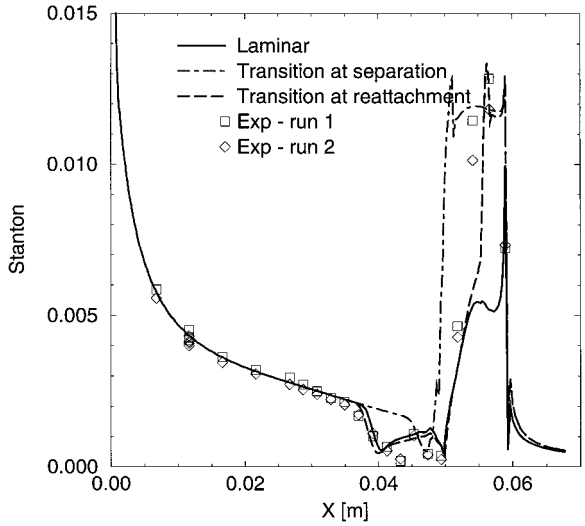

Fig. 15 Hyperboloid-flare computation: fine-grid Stanton number distributions.

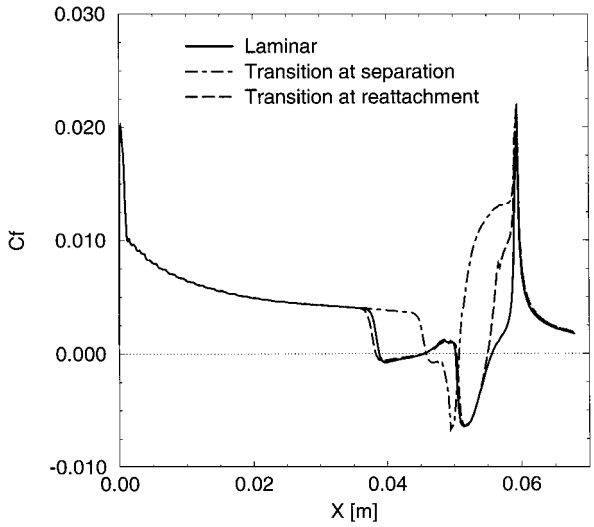

Fig. 16 Hyperboloid-flare computation: fine-grid skin-friction coefficient distributions.

Conclusion

The Spalart–Allmaras turbulence model has been implemented in a cell-centered finite volume solver and tested for several hypersonic flow configurations. For the fully attached nozzle flow case, as well as the hyperboloid-flare configuration that involves a laminar separation and turbulent reattachment, excellent agreement with the experimental data was obtained. For the hollow-cylinder flare configuration, which involves a turbulent separation, it was seen that peak pressure and heat transfer values could be correctly predicted if the mesh was appropriately designed, in particular if the resolution normal to the wall was sufficient, but the separation bubble size was underestimated.

This underestimation is believed to be an intrinsic limitation of the model. Indeed, the Spalart–Allmaras model, even if it is more sophisticated than other eddy viscosity models (for instance, the algebraic models), is designed mainly to treat attached flows. Moreover, because the production term b_{prod} is a function of the modulus of vorticity, the model presents a specific problem at points where the skin friction vanishes (separation and reattachment points). In fact, at such points, an artificial decrease in turbulent viscosity level is observed. This behavior is emphasized by the presence of damping terms, which are calibrated against the law of the wall and which do not apply in the neighborhood of separation or reattachment. Nevertheless, even if the behavior of the model in the separated flow regions is clearly off-design, the computed solution is able to provide important and useful information.

References

[1]Knight, D. D., and Degrez, G., "Shock Wave/Boundary Layer Interactions in High-Mach-Number Flows: A Critical Survey of Current CFD Prediction Capabilities," *Hypersonic Experimental and Computational Capability, Improvement and Validation*, Vol. 2, AGARD AR 319 (to be published).

[2]Baldwin, B. S., and Barth, T. J., "A One-Equation Turbulence Transport Model for High Reynolds Number Wall-Bounded Flows," AIAA Paper 91-0610, Jan. 1991.

[3]Spalart, P. R., and Allmaras, S. R., "A One-Equation Turbulence Model for Aerodynamic Flows," *La Recherche Aérospatiale*, No. 1, 1994, pp. 5–21.

[4]Papadakis, M., Lall, V., and Hoffman, K. A.,"Performance of Turbulence Models for Planar Flows: A Selected Review," AIAA Paper 94-1873, June 1994.

[5]Mensink, C., and Deconinck, H., "A 2D Multiblock Method for Viscous and Inviscid Flow Computations," *Proceedings of the IIIrd International Conference on Numerical Methods for Fluid Mechanics*, Oxford Univ. Press, Reading, England, UK, 1992.

[6]Broglia, R., Manna, M., Deconinck, H., and Degrez, G., "Development and Validation of an Axisymmetric Navier–Stokes Solver for Hypersonic Flows," von Kármán Inst., TN 188, Sint-Genesius-Rode, Belgium, May 1995.

[7]Paciorri, R., Deconinck, H., and Degrez, G., "Implementation and Validation of the Spalart–Allmaras Turbulence Model for Application in Hypersonic Flows," von Kármán Inst., TN 190, Sint-Genesius-Rode, Belgium, Jan. 1996.

[8]Schlichting, H., *Boundary Layer Theory*, 7th ed., McGraw–Hill, New York, 1979, pp. 543–546.

[9]Speziale, C. G., Abid, R., and Anderson, E. C., "Critical Evaluation of Two-Equation Models for Near-Wall Turbulence," *AIAA Journal*, Vol. 30, No. 2, 1992, pp. 311–326.

[10]Simeonides, G., "The VKI Hypersonic Wind Tunnels and Associated Measurements Techniques," von Kármán Inst., TM 46, Sint-Genesius-Rode, Belgium, Nov. 1990.

[11]Charbonnier, J.-M., Paris, S., and Dieudonné, W., "Extension of the Operating Domain of the VKI-Longshot Tunnel to the Use of Testing Gases with Various γ Values," 87th Supersonic Tunnel Association Meeting, von Kármán Inst., Reprint 1997-40, May 1997.

[12]Dieudonné, W., Charbonnier, J.-M., and Deconinck, H., "Nozzle Flow Sensitivity Analysis and Wind Tunnel Operating Envelope; Part II: Turbulent Case," von Kármán Inst., Contract TN HT-TN-E34-541-VKIN, Sint-Genesius-Rode, Belgium, April 1996.

[13]Délery, J., and Panaras, A. G., "Shock Wave/Boundary Layer Interactions in High-Mach-Number Flows," *Hypersonic Experimental and Computational Capability, Improvement and Validation*, Vol. 1, AGARD AR 319, 1996, pp. 2-1–2-61.

[14]Joulot, A., "Contribution à l'Étude de l'Interaction Onde de Choc-Couche Limite sur Rampe Bidimensionnelle en Régime Hypersonique," Ph.D. Thesis, Univ. Pierre et Marie Curie, Paris, 1992.

[15]Dolling, D., "Unsteady Phenomena in Shock-Wave/Boundary Layer Interaction," *AGARD/VKI Special Course on Shock-Wave Boundary-Layer Interactions in Supersonic and Hypersonic Flows*, von Kármán Inst. for Fluid Dynamics, AGARD R-792, Sint-Genesius-Rode, Belgium, 1993, pp. 4-1–4-46.

[16]Krogman, P., "Hyperboloid Flare Experiments at Mach 6.8 in RWG," DLR, German Aerospace Research Establishment, Contract TN HT-NT-O-2074-DLR, Göttingen, Germany, Sept. 1994.

[17]Simeonides, G., "Test Cases for CFD Code Validation for Inlets and Nozzles of Airbreathing Propulsion Systems," European Space Agency/European Space Research and Technology Center, ESA/ESTEC Doc. EWP/1784, Noordwijk, The Netherlands, June 1994.

[18]Dieudonné, W., Charbonnier, J.-M., and Deconinck, H., "Hyperboloid-Flare Standard Model at RWG Reference Calibration Points," von Kármán Inst., Contract TN HT-TN-E34-622-VKIN, Sint-Genesius-Rode, Belgium, May 1996.

[19]Dieudonné, W., Charbonnier, J.-M., and Deconinck, H., "Test Case III.B: Hyperboloid-Flare Standard Model at RWG Reference Calibration Points," European Space Agency/European Space Research and Technology Center Workshop 1996 on Aerothermodynamics and Ground to Flight Extrapolation, Noordwijk, The Netherlands, 1996; also von Kármán Inst., Reprint 1996-24, May 1996.

[20]Baldwin, B. S., and Lomax, H., "Thin Layer Approximation and Algebraic Model for Separated Turbulent Flows," AIAA Paper 78-257, Jan. 1978.

J. R. Maus
Associate Editor